Realizing high thermoelectric performance in *n*-type SnSe polycrystals *via* (Pb, Br) co-doping and multi-nanoprecipitates synergy

Wen-Hao Gu[1], Yi-Xin Zhang[1], Jun Guo[1], Jian-Feng Cai[1], Yu-Ke Zhu[1], Fengshan Zheng[2], Lei Jin[2], Jingtao Xu[3], Jing Feng[1] and Zhen-Hua Ge[1]**

1. Faculty of Materials Science and Engineering, Kunming University of Science and Technology, Kunming, 650093, China.

2. Ernst Ruska-Centre for Microscopy and Spectroscopy with Electrons and Peter Grünberg Institute, Forschungszentrum Jülich GmbH, 52425 Jülich, Germany.

3. Ningbo Ruiling Advanced Energy Materials Institute Co., Ltd, Ningbo 315500, China.

Corresponding authors: zge@kmust.edu.cn (Z.-H. Ge) l.jin@fz-juelich.de（L. Jin）

Abstract

Both *p*- and *n*-type single crystals SnSe have been reported to possess high performance thermoelectric performances, thus highlighting the possibility for commercialization. Polycrystalline SnSe has better mechanical properties however possesses inferior thermoelectric properties compared to single crystal SnSe. In this work, *n*-type polycrystalline $SnSe_{0.95}$ + *x* wt% $PbBr_2$ (*x* = 0, 0.5, 1, and 1.5) samples were synthesized by combining mechanical alloying and spark plasma sintering technology. The effects of $PbBr_2$ doping on thermoelectric performance of SnSe were studied in detail. The results show that the carrier concentration was dramatically increased from 2.51×10^{17} cm^{-3} in pure $SnSe_{0.95}$ to 1.79×10^{19} cm^{-3} in $SnSe_{0.95}$ + 1.5 wt% $PbBr_2$, further resulting in an enhanced electrical conductivity. Multi-nanoprecipitates are present in the samples, including SnO,

SnPb and $SnBr_xO_y$, which possibly affect the Seebeck coefficient and the lattice thermal conductivity. A peak *ZT* value of 1.1 was obtained at 773 K for the $SnSe_{0.95}$ + 1.0 wt% $PbBr_2$ sample. This work highlights that $PbBr_2$ is an effective dopant to improve the TE performance of *n*-type polycrystalline SnSe.

Keywords: polycrystalline SnSe; thermoelectric; carrier concentration; $PbBr_2$; Multi-Nanoprecipitates.

Introduction

Thermoelectric (TE) devices enable direct conversion between thermal and electrical energy. TE effect has thus attracted wide attention as an alternative green power generation methods.[1] In addition to power generation, TE materials also have huge potential in the field of solid refrigeration.[2-5] In practice, in working TE devices, *p*-type and *n*-type semiconductor pellets are connected by shunts, in order to form an tandem electric circuit.[1] Therefore, high TE performances of both *p*-type and *n*-type materials are required to construct efficient TE devices. Conversion efficiency of TE materials is generally characterized by a dimensionless figure of merit and can be expressed as follows:

$$ZT=\frac{S^2\sigma}{\kappa}T, \quad (1)$$

where S is the Seebeck coefficient, σ is the electrical conductivity, T is the absolute temperature, and κ is the total thermal conductivity including contributions from lattice vibration (κ_{lat}) and carriers transportation (κ_{ele}). High ZT therefore requires high power factor ($PF=S^2\sigma$) and low thermal conductivity. However, due to the inter-coupling between various TE parameters, it is difficult to manipulate each parameter independently. A variety of effective methods have been utilized to partially decouple these parameters to achieve the increased PF value and the decreased thermal conductivity over the past decades, such as the introduction of crystal defects,[6,7] nano-crystallization[8-10] and structural disorder[3,11] that could enhance phonon scattering to reduce lattice thermal conductivity, or through resonance doping, energy filtering effect and energy band degeneracy to achieve the simultaneous increase of Seebeck coefficient and electrical conductivity.[12-18] In addition to various optimization strategies, the discovery of materials with inherently excellent TE properties is also an effective way. Recently, a large number of new TE

material systems have been discovered and attracted great interest, including SnSe,[19-22] $Sb_2Si_2Te_6$,[23,24] Cu_2Se,[25-27] Mg_3Bi_2.[28,29] In particular, SnSe has increasingly attracted attention due to its intrinsic ultralow thermal conductivity. [21,30,31]

SnSe possesses anisotropy in thermoelectric properties along the ***a***, ***b*** and ***c*** axes due to its layered structure. In 2014, Zhao *et al*. reported that the *ZT* of single-crystal SnSe at 923 K was as high as 2.6 along the ***b*** axis, mainly as a result of the presence of non-harmonic bonds in the SnSe, thus leading in its ultra-low thermal conductivity (< 0.4 $Wm^{-1}K^{-1}$ at 923 K).[21] The *n*-type single crystal SnSe doped with Br has an ultra-high *ZT* value of 2.8 at 773 K in the out-of-plane.[22] However, the inferior mechanical performances of SnSe single crystal, as well as its time-consuming fabrications prevent its further developments and applications. Great effort has therefore been devoted to synthesize and optimize of TE performances of polycrystalline SnSe. For example, in *p*-type polycrystalline SnSe, cation doping has been adopted to increase the carrier concentration effectively.[32,33] Halogens, such as Cl, Br and I, have proven to be the effective dopants for *n*-type SnSe.[34-36] Br doping can greatly increase the carrier concentration of *n*-type polycrystalline SnSe and is considered to be the most effective doping strategy. In addition, the doping of I and Cl has also been attempted as a feasible optimization method. Zhang *et al*. and Cha *et al*. have reported that with an increasing content of I and Cl, the carrier concentration changes from 2.3×10^{17} cm^{-3} (*p*-type) to 2.4×10^{17} cm^{-3} (*n*-type) in $SnSe_{0.96}I_{0.04}$, and the carrier concentration of $SnSe_{0.95}Cl_{0.05}$ increases to 4.5×10^{18} cm^{-3} when Cl is used.[35,36] Similarly, halide doping is also a feasible method to optimize *n*-type SnSe. Li *et al*. and Wang *et al*. have reported significant increases in carrier concentration through $PbBr_2$ and $BiCl_3$ doping, ranging from 10^{17} to 10^{19} cm^{-3}.[37,38] Chang *et al*. has reported that through Br doping and Pb alloying, the *PF* can be improved with the thermal conductivity

unchanged, thus leading to a maximum *ZT* value of 1.2 at 773 K for $Sn_{0.9}Pb_{0.1}Se_{0.97}Br_{0.03}$ samples.[39] However, the mechanism of enhanced TE properties of $PbBr_2$ doped SnSe was not discussed in detail, in particular on the microstructural evidence. Due to a small electronegativity difference between Pb and Sn, it is expected that the doping of Pb will result in a higher carrier concentration.[40] The mass fluctuation caused by the introduction of Pb atoms simultaneously enhance phonon scattering in SnSe.[37] In addition, the introduction of cation and anion at both Sn and Se sites by multi-step doping or co-doping is also an effective way to improve the *ZT* value of SnSe.[37,39]

Similar to the previous work, the introduction of Se vacancies before doping enables the switch from *p*-type to *n*-type of polycrystalline SnSe. In this study, polycrystalline $SnSe_{0.95}$ + *x* wt% $PbBr_2$ (*x* = 0, 0.5, 1, and 1.5) samples were synthesized by a fast process, mechanical alloying (MA) combined with spark plasma sintering (SPS). SnSe undergoes a displacive (shear) phase transition at ~780 K, switching between a high-temperature higher symmetry phase (*Cmcm*, #63) and a low-temperature lower symmetry (*Pnma*, #62).[41] Results show that the carrier concentration has been enhanced remarkably from 2.51×10^{17} cm^{-3} for undoped SnSe to 1.79×10^{19} cm^{-3} for $SnSe_{0.95}$ + 1.5 wt% $PbBr_2$. The peak value of *PF* lifts up prominently from 17.9 $Wm^{-1}K^{-2}$ for $SnSe_{0.95}$ to 532.2 $Wm^{-1}K^{-2}$ for $SnSe_{0.95}$ + 1.5 wt% $PbBr_2$ at 773 K. The microstructures of SnSe samples have then been investigated in detail by spherical-aberration-corrected scanning transmission electron microscopy (C_S-STEM), revealing multi-nanoprecipitates in SnSe samples after $PbBr_2$ doping. With the increasing content of $PbBr_2$, the thermal conductivity reduces from 0.39 $Wm^{-1}K^{-1}$ to 0.32 $Wm^{-1}K^{-1}$. These improvements thus lead to a maximum *ZT* of 1.1 for the $SnSe_{0.95}$ + 1.0 wt% $PbBr_2$ at 773 K.

Materials and Methods

Polycrystalline $SnSe_{0.95}$ + x wt% $PbBr_2$ (x = 0, 0.5, 1, and 1.5) samples were synthesized by mechanical alloying with a mole ratio of high-purity Sn (powder, 99.99%) and Se (powder, 99.99%). The $SnSe_{0.95}$ powders were obtained by planetary ball mill (QM-3SP2, Nanjing University, China) with a rotating speed of 425 rpm for 8 hours. $SnSe_{0.95}$ and $PbBr_2$ powders were then mixed by planetary ball mill for 1 hour. The mixture was filled moderately into graphite die with a diameter of Φ15 mm, followed by spark plasma sintering (Sumitomo SPS211-X, Japan) that was used to process the mixed powders with 50 MPa at 773 K for 5 min.

The density ρ was measured by an Archimedes method, and the phase structure of the sample was analyzed by X-ray diffraction (XRD, MiniFlex600 Rigaku, Japan). Microstructures of the samples were investigated by high-angle annular dark-field imaging (HAADF) STEM in a C_S-corrected FEI Titan microscope operated at 200 kV. The chemical information of the samples was further studied using energy dispersive X-ray spectroscopy (EDX, Bruker Super-X). The Hall coefficients of all samples were measured using the van der Pauw technique under a reversible magnetic field of 0.80 T (8400 Series, Model 8404, Lake Shore, Watertown, IL, USA). The carrier concentration n and mobility μ were calculated by $n = 1/(eR_H)$ and $\mu = \sigma R_H$, respectively. The electrical conductivity (σ) and Seebeck coefficient (S) of all samples were measured (ZEM-3, ULVAC-RIKO, Japan) in a rarefied helium atmosphere from 323 to 773 K. The total thermal conductivity was calculated using the formula $\kappa = D\rho C_p$, where D and C_p are the thermal diffusivity and the heat capacity, respectively. The thermal diffusivity (D) was measured by laser flash method (LFA 457, NETZSCH LFA, Germany) in an argon atmosphere using Cowan model plus pulse correction. The heat capacity (C_p) was taken from previously reported literature.[21] The uncertainty of each measurement was around 5%, resulting in an error of about 20% in ZT.

Results and discussions

Figure 1 shows the XRD patterns of $SnSe_{0.95}$ + *x* wt% $PbBr_2$ (*x* = 0, 0.5, 1, and 1.5) of all samples that were measured at room temperature. All the patterns can be indexed to the low temperature SnSe phase (JCPDS #48-1224) with an orthorhombic structure. It belongs to space group #62, *Pnma* and lattice constants are *a*=11.49 Å, *b*=4.135Å and *c*=4.44Å.[7] The diffraction peaks around 32 ° and 45 ° of $SnSe_{0.95}$ sample are indexed to elemental Sn (JCPDS #86-2264),[35] but disappeared in the doped samples. The diffraction peak belonging to SnO (JCPDS #24-1342) was observed in each doped sample, indicating that the $PbBr_2$ doping may make the Sn oxidization in the synthesis process. The XRD results also reveal that the diffraction peaks continuously shift towards the lower angles with the increasing $PbBr_2$ content, suggesting that Pb^{2+} enters the matrix lattice and then substitute Sn^{2+}, thus causing the lattice to expand, as the ion radius of Pb^{2+} (1.49 Å) is larger than that of Sn^{2+} (1.22 Å). Since the ionic radii of Se^{2-} (1.98 Å) and Br^- (1.96 Å) are pretty close, Br has little effect on the lattice parameters.[39] In addition, it is obvious that the (400) peak is obviously stronger than the (111) peak, indicating anisotropy in the sample with a preferred orientation along the (400) plane.[42] The orientation factor of (400) crystal plane, *F*(400), can be calculated using the Lotgering method[43,44]

$$F = \frac{P - P_0}{1 - P_0} \quad (2)$$

$$P = \frac{I(400)}{\sum I(hkl)} \quad (3)$$

$$P_0 = \frac{I_0(400)}{\sum I_0(hkl)} \quad (4)$$

where *P* and P_0 are the ratio between integrated intensities of the (400) planes and the intensities of all (*hkl*) planes for preferentially- and randomly-oriented samples, within the range of 20-60 °, respectively. When the value of *F*(400) is 1, it indicates that the ***a*** axis in the grain is just in the

direction of the parallel pressure.[42] In this work, the calculated value of $F(400)$ is about 0.3, suggesting that the axial plane is slightly preferentially oriented in the *bc* plane.

The microstructure of the sample ($SnSe_{0.95}$ + 1.0 wt% $PbBr_2$) with the highest TE performance was investigated using C_S-STEM. The measured lattice spacings are 0.287 and 0.4 nm, respectively, which are consistent with the (400) and $(0\bar{1}1)$ planes of SnSe, as shown in Figure 2a. In the enlarged part of Figure 2b and Figure 2c, the green and red spheres represent Sn and Se, respectively. In Figure 2c, a partially-coherent grain boundary is observed and marked by a dashed line. Such grains can effectively scatter phonons. Figures 2d-f are HAADF image and corresponding elemental maps of $SnSe_{0.95}$ + 1.0 wt% $PbBr_2$. It is evident that Sn and O are clustered in the same region, as inferred from XRD, indicating that SnO precipitates aggregate in the sample $SnSe_{0.95}$ + 1.0 wt% $PbBr_2$ substrate. According the XRD results, the $PbBr_2$ doping is the main reason for the formation of SnO because that there is not SnO but only element Sn in the $SnSe_{0.95}$ sample. The Pb and/or Br doping may decrease the formation energy from Sn to SnO, that is, the Pb and/or Br doping make Sn easier to be oxidized in the synthesis process. Figure 3 shows HAADF STEM images together with EDX elemental maps. The aggregation of O and Sn can be seen as marked by the red solid line in Figure 3c and 3f, respectively, indicating that SnO mainly existed in the grain boundaries. Besides SnO, there are also multi-precipitates at grain boundaries as shown in Figure 3. These precipitates can act as phonon scattering centers and further reduce the lattice thermal conductivity. The enrichment of Sn and Pb can be observed as shown in Figure 3d and 3f (see white lines), indicating that there is a small quantity of two-phase alloying of Sn and Pb in the sample. In addition, the three-phase compound of $SnBr_xO_y$ can be observed in Figure 3b, 3c and 3f (see yellow lines). It can be seen in Figure 3g-3k that Pb and Br uniformly distribute in the $SnSe_{0.95}$ + 1.0 wt% $PbBr_2$ sample, suggesting

that $PbBr_2$ is effectively doped into the matrix by atomic diffusion.

The electrical transport properties of $SnSe_{0.95}$ + x wt% $PbBr_2$ (x = 0, 0.5, 1, and 1.5) samples were measured along the direction parallel to the SPS pressing direction. As shown in Figure 4a, the electrical conductivities of all samples increases with the temperature, indicating typical semiconductor characteristics. In particular, the electrical conductivity of undoped $SnSe_{0.95}$ sample increases from 8.53 × 10^{-4} S·cm^{-1} at room temperature to 6.38 S·cm^{-1} at 773 K. Such a giant increase of electrical conductivity with four orders of magnitude is similar to previous reports.[45] With $PbBr_2$ doping, the electrical conductivity of the sample is further improved. The maximum electrical conductivity at room temperature is boosted to approximately 0.2 S·cm^{-1} in the $SnSe_{0.95}$ + 1.5 wt % $PbBr_2$ sample. The electrical conductivity of all doped samples increases sharply in the range between 573 and 773 K. The maximum electrical conductivity of $SnSe_{0.95}$ + 1.5 wt % $PbBr_2$ is 32.8 S·cm^{-1}, which is 5 times higher than that of undoped sample at the same temperature. In order to further explain the reason why the electrical conductivity increases with the $PbBr_2$ doping concentration, the Hall carrier concentration and mobility are then measured at room temperature, as displayed in Figure 4b. Compared with the undoped sample, the carrier concentration of the 1.5 wt% $PbBr_2$-doped sample is enhanced by two orders of magnitude, from 2.51×10^{17} cm^{-3} to 1.79×10^{19} cm^{-3}. This is mainly because Br^- enters the matrix lattice to replace Se^{2-} and release an electron, and the doping mechanism can be described using the following formula.

$$Sn + O + V_{\ddot{S}n} + 2V_{\ddot{S}e} + PbBr_2 \rightarrow Pb_{\dot{S}n}^{\times} + 2Br_{\dot{S}e} + \mathrm{SnO} \quad (5)$$

The result further evidences that $PbBr_2$ is an effective dopant to increase the electrical conductivity of *n*-type SnSe.

Figure 4c shows the relationship between Seebeck coefficient and temperature for all samples.

The matrix sample underwent *p*-*n* switch at 523 K, as reported elsewhere.[37] In the whole measured temperature range, the Seebeck coefficient of all the doped samples are negative, indicating *n*-type semiconductors. The $SnSe_{0.95}$ + 0.5 wt% $PbBr_2$ sample exhibits an optimal *S* value of – 466 μVK^{-1} at 323 K, which is dramatically enhanced compared with that of the undoped $SnSe_{0.95}$. In addition, in the whole measurement temperature range, the *PF* of all the doped samples increases with temperature, as shown in Figure 4d. The maximum *PF* of the sample $SnSe_{0.95}$ with 1.5 wt% $PbBr_2$ doping at 773 K is 532 $\mu Wm^{-1}K^{-2}$, which is about 30 times higher than that of the undoped sample and also higher than that in other polycrystalline *n*-type SnSe.[34,39]

Figure 5 shows the thermal transport properties of all samples $SnSe_{0.95}$ + *x* wt% $PbBr_2$ (*x* = 0, 0.5, 1, and 1.5) as a function of temperature. The total thermal conductivity (κ_{tot}) comprises contributions from carriers and phonons and can be expressed by the formula $\kappa_{tot} = \kappa_{lat} + \kappa_{ele}$, where the electron thermal conductivity (κ_{ele}) can be calculated by the Wiedemann–Franz law $\kappa_{ele} = L\sigma T$ (*L* is the Lorenz number).[46-48] The lattice thermal conductivity, as shown in Figure 5c, is seen to be dominant in the total thermal conductivity, as a result of a low carrier concentration, only 10^{19} cm^{-3} after doping. The thermal conductivity (Figure 5a) of all samples decreases with temperature due to the intrinsic excitations of phonons. For the undoped $SnSe_{0.95}$ sample, the thermal conductivity reduces from 1.06 $Wm^{-1}K^{-1}$ at room temperature to 0.39 $Wm^{-1}K^{-1}$ at 773 K. After introducing $PbBr_2$, the thermal conductivity drops, with a minimum of 0.32 $Wm^{-1}K^{-1}$ at 773 K in the $SnSe_{0.95}$ + 0.5 wt % $PbBr_2$ specimen. Such reduction in $PbBr_2$-doped samples can be ascribed to the introduction of multiple nano-precipitates, as hinted from microstructural observations. Although the SnO phase with high thermal conductivity is detected, there are also other types of associated precipitates in the samples, such as the Sn-Pb alloy and $SnBr_xO_y$ compound. The introduced extra phase boundaries

could be regarded as phonon scattering centers to significantly inhibit the propagation of phonons, thus reducing the lattice thermal conductivity. Furthermore, the introduced point defects by doping could distort the lattice symmetry, especially by the heavier and larger Pb^{2+} ions doping, which is beneficial for scattering the short-wavelength phonons and results in a low thermal conductivity.

Figure 6a shows the temperature-dependent *ZT* for the $SnSe_{0.95}$ + *x* wt% $PbBr_2$ (*x* = 0, 0.5, 1, and 1.5) samples. For the undoped $SnSe_{0.95}$, the maximum *ZT* (ZT_{max}) value is 0.03 at 773 K, while for the $SnSe_{0.95}$ + 1.0 wt% $PbBr_2$ sample, the ZT_{max} was 1.1 at 773 K, two orders of magnitude compared with that of the undoped $SnSe_{0.95}$. The $SnSe_{0.95}$ + 1.0 wt% $PbBr_2$ sample was re-prepared, and its thermoelectric properties were measured during heating and cooling. The sample with good stability has been confirmed by the TE performance cycling measurement results (see Fig. S1-S2). Figure 6b shows ZT_{max} comparison with reported values of other *n*-type polycrystalline SnSe in the literature.[35-39,45,49-54] It is seen that $PbBr_2$-doping is also an effective approach for *n*-type SnSe that can optimize its TE performances.

Conclusion

In summary, *n*-type polycrystalline $SnSe_{0.95}$ + *x* wt% $PbBr_2$ (*x* = 0, 0.5, 1, and 1.5) samples were prepared by combing MA process and SPS technique. With the increase of $PbBr_2$ content, the carrier concentration of SnSe sample increases from 2.51×10^{17} cm^{-3} in the undoped $SnSe_{0.95}$ to 1.79×10^{19} cm^{-3} in $SnSe_{0.95}$ + 1.0 wt % $PbBr_2$, showing the $PbBr_2$ is an effective electron dopant for SnSe system. Benefiting from the increased carrier concentration, the electrical conductivity and power factor are thus enhanced. The introduction of multi-nanoprecipitates, including SnO, SnPb and $SnBr_xO_y$, further reduces the lattice thermal conductivity. The maximum *ZT* value of 1.1 at 773 K is therefore achieved in $SnSe_{0.95}$ + 1.0 wt % $PbBr_2$ along the direction of parallel SPS pressure.

Acknowledgement

This work was supported by the National Natural Science Foundation of China (Grant No. 11764025).

Refference

[1] L.E. Bell, Cooling, heating, generating power, and recovering waste heat with thermoelectric systems, science. 321 (2008) 1457-1461.

[2] F.J. DiSalvo, Thermoelectric cooling and power generation, Science. 285 (1999) 703-706.

[3] G.J. Snyder, E.S. Toberer, Complex thermoelectric materials, Nat. Mater. 7 (2008) 105-114.

[4] T.M. Tritt, Holey and unholey semiconductors, Science. 283 (1999) 804-805.

[5] N. Wang, L. Han, H. He, N.-H. Park, K. Koumoto, A novel high-performance photovoltaic–thermoelectric hybrid device, Energy Environ. Sci. 4 (2011) 3676-3679.

[6] H. Zhao, J. Sui, Z. Tang, Y. Lan, Q. Jie, D. Kraemer, K. McEnaney, A. Guloy, G. Chen, Z. Ren, High thermoelectric performance of MgAgSb-based materials, Nano Energy. 7 (2014) 97-103.

[7] Z.-H. Ge, D. Song, X. Chong, F. Zheng, L. Jin, X. Qian, L. Zheng, R.E. Dunin-Borkowski, P. Qin, J. Feng, Boosting the thermoelectric performance of (Na, K)-codoped polycrystalline SnSe by synergistic tailoring of the band structure and atomic-scale defect phonon scattering, J. Am. Chem. Soc. 139 (2017) 9714-9720.

[8] B. Poudel, Q. Hao, Y. Ma, Y. Lan, A. Minnich, B. Yu, X. Yan, D. Wang, A. Muto, D. Vashaee, High-thermoelectric performance of nanostructured bismuth antimony telluride bulk alloys, Science. 320 (2008) 634-638.

[9] K. Biswas, J. He, I.D. Blum, C.-I. Wu, T.P. Hogan, D.N. Seidman, V.P. Dravid, M.G. Kanatzidis, High-performance bulk thermoelectrics with all-scale hierarchical architectures, Nature. 489 (2012) 414-418.

[10] W. Liu, J. Hu, S. Zhang, M. Deng, C.-G. Han, Y. Liu, New trends, strategies and opportunities in thermoelectric materials: a perspective, Mater. Today Phys. 1 (2017) 50-60.

[11] B. Li, H. Wang, Y. Kawakita, Q. Zhang, M. Feygenson, H. Yu, D. Wu, K. Ohara, T. Kikuchi, K. Shibata, Liquid-like thermal conduction in intercalated layered crystalline solids, Nat. Mater. 17 (2018) 226-230.

[12] Y. Pei, X. Shi, A. LaLonde, H. Wang, L. Chen, G.J. Snyder, Convergence of electronic bands for high performance bulk thermoelectrics, Nature. 473 (2011) 66-69.

[13] S.N. Girard, J. He, X. Zhou, D. Shoemaker, C.M. Jaworski, C. Uher, V.P. Dravid, J.P. Heremans, M.G. Kanatzidis, High performance Na-doped PbTe–PbS thermoelectric materials: electronic density of states modification and shape-controlled nanostructures, J. Am. Chem. Soc. 133 (2011) 16588-16597.

[14] Y. Pei, A.D. LaLonde, N.A. Heinz, X. Shi, S. Iwanaga, H. Wang, L. Chen, G.J. Snyder, Stabilizing the optimal carrier concentration for high thermoelectric efficiency, Adv. Mater. 23 (2011) 5674-5678.

[15] J.P. Heremans, V. Jovovic, E.S. Toberer, A. Saramat, K. Kurosaki, A. Charoenphakdee, S. Yamanaka, G.J. Snyder, Enhancement of thermoelectric efficiency in PbTe by distortion of the electronic density of states, Science. 321 (2008) 554-557.

[16] Q. Zhang, H. Wang, W. Liu, H. Wang, B. Yu, Q. Zhang, Z. Tian, G. Ni, S. Lee, K. Esfarjani, Enhancement of thermoelectric figure-of-merit by resonant states of aluminium doping in lead selenide, Energy Environ. Sci. 5 (2012) 5246-5251.

[17] J.P. Heremans, B. Wiendlocha, A.M. Chamoire, Resonant levels in bulk thermoelectric semiconductors, Energy Environ. Sci. 5 (2012) 5510-5530.

[18] C.M. Jaworski, B. Wiendlocha, V. Jovovic, J.P. Heremans, Combining alloy scattering of phonons and resonant electronic levels to reach a high thermoelectric figure of merit in PbTeSe and

PbTeS alloys, Energy Environ. Sci. 4 (2011) 4155-4162.

[19] L. Mao, Y. Yin, Q. Zhang, G. Liu, H. Wang, Z. Guo, H. Hu, Y. Xiao, X. Tan, J. Jiang, Fermi-surface dynamics and High thermoelectric performance along the out-of-plane direction in *n*-type SnSe crystal, Energy Environ. Sci. 13 (2020) 616-621.

[20] Y. Zhu, J. Carrete, Q.-L. Meng, Z. Huang, N. Mingo, P. Jiang, X. Bao, Independently tuning the power factor and thermal conductivity of SnSe via Ag_2S addition and nanostructuring, J. Mater. Chem. A. 6 (2018) 7959-7966.

[21] L.-D. Zhao, S.-H. Lo, Y. Zhang, H. Sun, G. Tan, C. Uher, C. Wolverton, V.P. Dravid, M.G. Kanatzidis, Ultralow thermal conductivity and high thermoelectric figure of merit in SnSe crystals, Nature. 508 (2014) 373-377.

[22] C. Chang, M. Wu, D. He, Y. Pei, C.-F. Wu, X. Wu, H. Yu, F. Zhu, K. Wang, Y. Chen, 3D charge and 2D phonon transports leading to high out-of-plane ZT in *n*-type SnSe crystals, Science. 360 (2018) 778-783.

[23] Y. Luo, S. Cai, S. Hao, F. Pielnhofer, I. Hadar, Z.-Z. Luo, J. Xu, C. Wolverton, V.P. Dravid, A. Pfitzner, High-performance thermoelectrics from cellular nanostructured $Sb_2Si_2Te_6$, Joule. 4 (2020) 159-175.

[24] Z. Huang, L.-D. Zhao, Sb2Si2Te6: A robust new thermoelectric material, Trends Chem. 2 (2020) 89-91.

[25] A. Olvera, N. Moroz, P. Sahoo, P. Ren, T. Bailey, A. Page, C. Uher, P. Poudeu, Partial indium solubility induces chemical stability and colossal thermoelectric figure of merit in Cu_2Se, Energy Environ. Sci. 10 (2017) 1668-1676.

[26] R. Nunna, P. Qiu, M. Yin, H. Chen, R. Hanus, Q. Song, T. Zhang, M.-Y. Chou, M.T. Agne, J. He,

Ultrahigh thermoelectric performance in Cu_2Se-based hybrid materials with highly dispersed molecular CNTs, Energy Environ. Sci. 10 (2017) 1928-1935.

[27] L. Yang, Z.-G. Chen, G. Han, M. Hong, L. Huang, J. Zou, Te-Doped Cu_2Se nanoplates with a high average thermoelectric figure of merit, J. Mater. Chem. A. 4 (2016) 9213-9219.

[28] J. Mao, H. Zhu, Z. Ding, Z. Liu, G.A. Gamage, G. Chen, Z. Ren, High thermoelectric cooling performance of *n*-type Mg_3Bi_2-based materials, Science. 365 (2019) 495-498.

[29] T.R. Chang, I. Pletikosic, T. Kong, G. Bian, A. Huang, J. Denlinger, S.K. Kushwaha, B. Sinkovic, H.T. Jeng, T. Valla, Realization of a Type- II Nodal- Line Semimetal in Mg_3Bi_2, Adv. Sci. 6 (2019) 1800897.

[30] L.-D. Zhao, G. Tan, S. Hao, J. He, Y. Pei, H. Chi, H. Wang, S. Gong, H. Xu, V.P. Dravid, Ultrahigh power factor and thermoelectric performance in hole-doped single-crystal SnSe, Science. 351 (2016) 141-144.

[31] C.W. Li, J. Hong, A.F. May, D. Bansal, S. Chi, T. Hong, G. Ehlers, O. Delaire, Orbitally driven giant phonon anharmonicity in SnSe, Nat. Phys. 11 (2015) 1063-1069.

[32] Y. Zhu, J. Carrete, Q.-L. Meng, Z. Huang, N. Mingo, P. Jiang, X. Bao, Independently tuning the power factor and thermal conductivity of SnSe via Ag_2S addition and nanostructuring, J. Mater. Chem. A. 6 (2018) 7959-7966.

[33] Q. Zhao, B. Qin, D. Wang, Y. Qiu, L.-D. Zhao, Realizing High Thermoelectric Performance in Polycrystalline SnSe via Silver Doping and Germanium Alloying, ACS Appl. Energy Mater. 3 (2019) 2049-2054.

[34] S. Li, Y. Wang, C. Chen, X. Li, W. Xue, X. Wang, Z. Zhang, F. Cao, J. Sui, X. Liu, Heavy Doping by Bromine to Improve the Thermoelectric Properties of *n*- type Polycrystalline SnSe, Adv.

Sci. 5 (2018) 1800598.

[35] J. Cha, C. Zhou, Y.K. Lee, S.-P. Cho, I. Chung, High Thermoelectric Performance in *n*-Type Polycrystalline SnSe via Dual Incorporation of Cl and PbSe and Dense Nanostructures, ACS Appl. Mater. Interfaces. 11 (2019) 21645-21654.

[36] Q. Zhang, E.K. Chere, J. Sun, F. Cao, K. Dahal, S. Chen, G. Chen, Z. Ren, Studies on thermoelectric properties of *n*- type polycrystalline $SnSe_{1-x}S_x$ by iodine doping, Adv. Energy Mater. 5 (2015) 1500360.

[37] D. Li, X. Tan, J. Xu, G. Liu, M. Jin, H. Shao, H. Huang, J. Zhang, J. Jiang, Enhanced thermoelectric performance in *n*-type polycrystalline SnSe by $PbBr_2$ doping, RSC Adv. 7 (2017) 17906-17912.

[38] X. Wang, J. Xu, G. Liu, Y. Fu, Z. Liu, X. Tan, H. Shao, H. Jiang, T. Tan, J. Jiang, Optimization of thermoelectric properties in *n*-type SnSe doped with $BiCl_3$, Appl. Phys. Lett. 108 (2016) 083902.

[39] C. Chang, Q. Tan, Y. Pei, Y. Xiao, X. Zhang, Y.-X. Chen, L. Zheng, S. Gong, J.-F. Li, J. He, Raising thermoelectric performance of *n*-type SnSe via Br doping and Pb alloying, RSC Adv. 6 (2016) 98216-98220.

[40] G. Tang, W. Wei, J. Zhang, Y. Li, X. Wang, G. Xu, C. Chang, Z. Wang, Y. Du, L.-D. Zhao, Realizing High Figure of Merit in Phase-Separated Polycrystalline $Sn_{1-x}Pb_xSe$, J. Am. Chem. Soc. 138 (2016) 13647-13654.

[41] S. Sassi, C. Candolfi, J.-B. Vaney, V. Ohorodniichuk, P. Masschelein, A. Dauscher, B. Lenoir, Assessment of the thermoelectric performance of polycrystalline *p*-type SnSe, Appl. Phys. Lett. 104 (2014) 212105.

[42] F. Li, W. Wang, Z.-H. Ge, Z. Zheng, J. Luo, P. Fan, B. Li, Enhanced thermoelectric properties of

polycrystalline SnSe via $LaCl_3$ doping, Materials. 11 (2018) 203.

[43] F. Lotgering, Topotactical reactions with ferrimagnetic oxides having hexagonal crystal structures—I, J. Inorg. Nucl. Chem. 9 (1959) 113-123.

[44] L. Zhao, B.-P. Zhang, J.-F. Li, H. Zhang, W. Liu, Enhanced thermoelectric and mechanical properties in textured *n*-type Bi_2Te_3 prepared by spark plasma sintering, Solid State Sci. 10 (2008) 651-658.

[45] F. Li, W. Wang, X. Qiu, Z. Zheng, P. Fan, J. Luo, B. Li, Optimization of thermoelectric properties of *n*-type Ti, Pb co-doped SnSe, Inorg. Chem. Front. 4 (2017) 1721-1729.

[46] S. Perumal, S. Roychowdhury, D.S. Negi, R. Datta, K. Biswas, High thermoelectric performance and enhanced mechanical stability of *p*-type $Ge_{1-x}Sb_xTe$, Chem. Mater. 27 (2015) 7171-7178.

[47] S.N. Guin, A. Chatterjee, D.S. Negi, R. Datta, K. Biswas, High thermoelectric performance in tellurium free *p*-type $AgSbSe_2$, Energy Environ. Sci. 6 (2013) 2603-2608.

[48] L.-D. Zhao, S.-H. Lo, J. He, H. Li, K. Biswas, J. Androulakis, C.-I. Wu, T.P. Hogan, D.-Y. Chung, V.P. Dravid, High performance thermoelectrics from earth-abundant materials: enhanced figure of merit in PbS by second phase nanostructures, J. Am. Chem. Soc. 133 (2011) 20476-20487.

[49] J. Gainza, F. Serrano-Sánchez, M. Gharsallah, F. Carrascoso, J. Bermúdez, O. Dura, F. Mompean, N. Biskup, J. Meléndez, J. Martínez, Evidence of nanostructuring and reduced thermal conductivity in *n*-type Sb-alloyed SnSe thermoelectric polycrystals, J. Appl. Phys. 126 (2019) 045105.

[50] T. Shen, K.Y. Li, Z.J. Chen, H.F. Wu, J.X. Si, Enhanced Thermoelectric Performance of *n*-Type Polycrystalline SnSe via $MoCl_5$ Doping, J. Electron. Mater. 49 (2020) 621-626.

[51] S. Li, F. Zhang, C. Chen, X. Li, F. Cao, J. Sui, X. Liu, Z. Ren, Q. Zhang, Enhanced thermoelectric performance in polycrystalline N-type Pr-doped SnSe by hot forging, Acta Mater. 190 (2020) 1-7.

[52] Z.-H. Ge, Y. Qiu, Y.-X. Chen, X. Chong, J. Feng, Z.-K. Liu, J. He, Multipoint Defect Synergy Realizing the Excellent Thermoelectric Performance of *n*-Type Polycrystalline SnSe via Re Doping, Adv. Funct. Mater. 29 (2019) 1902893.

[53] J. Cai, Y. Zhang, Y. Yin, X. Tan, S. Duan, G.-Q. Liu, H. Hu, Y. Xiao, Z. Ge, J. Jiang, Investigating the thermoelectric performance of *n*-type SnSe: the synergistic effect of $NbCl_5$ doping and dislocation engineering, J. Mater. Chem. C. 8 (2020) 13244-13252.

[54] P.P. Shang, J. Dong, J. Pei, F.H. Sun, Y. Pan, H. Tang, B.P. Zhang, L.D. Zhao, J.F. Li, Highly Textured N-Type SnSe Polycrystals with Enhanced Thermoelectric Performance, Research. 2019 (2019) 9253132.

Figure captions

Figure 1. a) The XRD patterns of $SnSe_{0.95}$ + *x* wt% $PbBr_2$ (*x* = 0, 0.5, 1, and 1.5) samples and b) enlarged XRD patterns in the 2θ range from 30 ºto 32 º.

Figure 2. a, b, c) High-angle annular dark-field images of $SnSe_{0.95}$ + 1.0 wt% $PbBr_2$ samples recorded along the a,b) [011] and c) [001] axes. The inset to a) shows indexed electron diffraction patter and the insets to b, c) are magnified atomic images. d-g) High-angle annular dark-field image and corresponding energy dispersive X-ray spectroscopic maps of $SnSe_{0.95}$ + 1.0 wt% $PbBr_2$ showing the coexistence of SnSe and SnO precipitate.

Figure 3. a) High-angle annular dark-field image and b-f) corresponding EDX elemental maps for Br, O, Pb, Se and Sn were taken from a) for $SnSe_{0.95}$ + 1 wt% $PbBr_2$ sample, respectively, showing the presence of SnO, Pb-Sn and $SnBr_xO_y$ multi-precipitates. g) HAADF and h-k) corresponding elemental maps of $SnSe_{0.95}$ + 1 wt% $PbBr_2$ grain showing a uniform distribution of dopants.

Figure 4. Electrical transport properties as a function of temperature for all the samples $SnSe_{0.95}$ + *x* wt% $PbBr_2$ (*x* = 0, 0.5, 1, and 1.5). a) electrical conductivity, b) carrier concentration and mobility, c) Seebeck coefficient, d) *PF*.

Figure 5. Thermal transport properties as a function of temperature for all the samples $SnSe_{0.95}$ + *x* wt% $PbBr_2$ (*x* = 0, 0.5, 1, and 1.5). a) Thermal conductivity, b) electrical thermal conductivity, c) lattice thermal conductivity.

Figure 6. a) Temperature dependence of TE properties for the $SnSe_{0.95}$ + *x* wt% $PbBr_2$ (*x* = 0, 0.5, 1, and 1.5) samples and b) the ZT_{max} of the *n*-type polycrystalline Sn–Se system TE materials.[35-39,45,49-54]

Figures

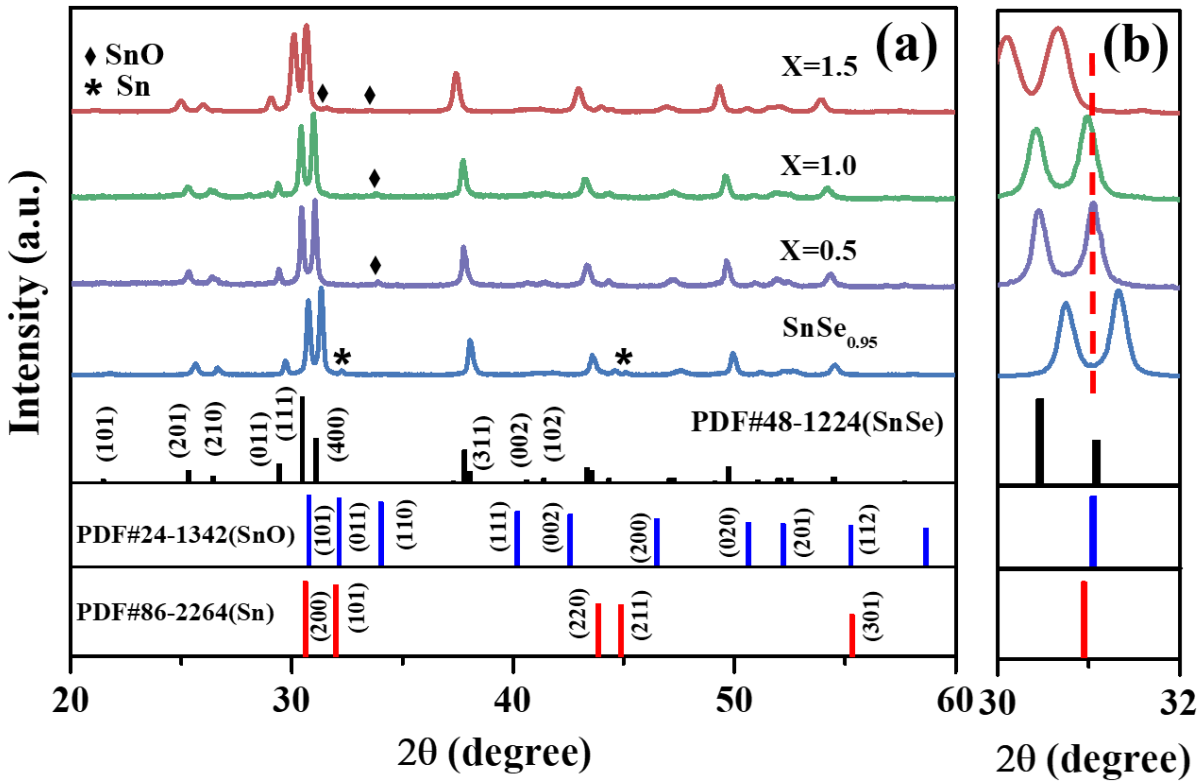

Figure 1.

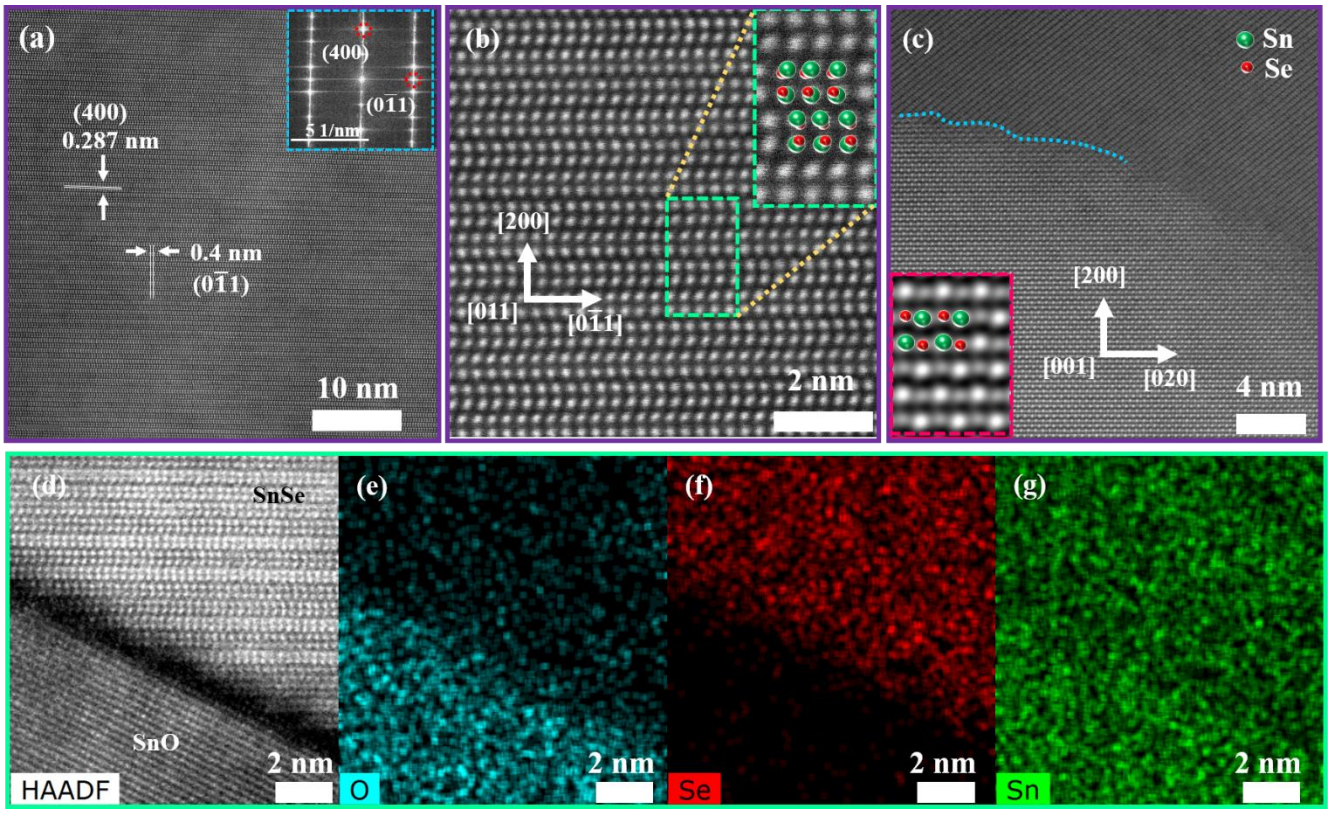
(a)
(400)
(01̄1)
5 1/nm
(400)
0.287 nm
0.4 nm
(01̄1)
10 nm
(b)
[200]
[011]
[01̄1]
2 nm
(c)
Sn
Se
[200]
[001]
[020]
4 nm
(d)
SnSe
SnO
2 nm
HAADF
(e)
2 nm
O
(f)
2 nm
Se
(g)
2 nm
Sn

Figure 2.

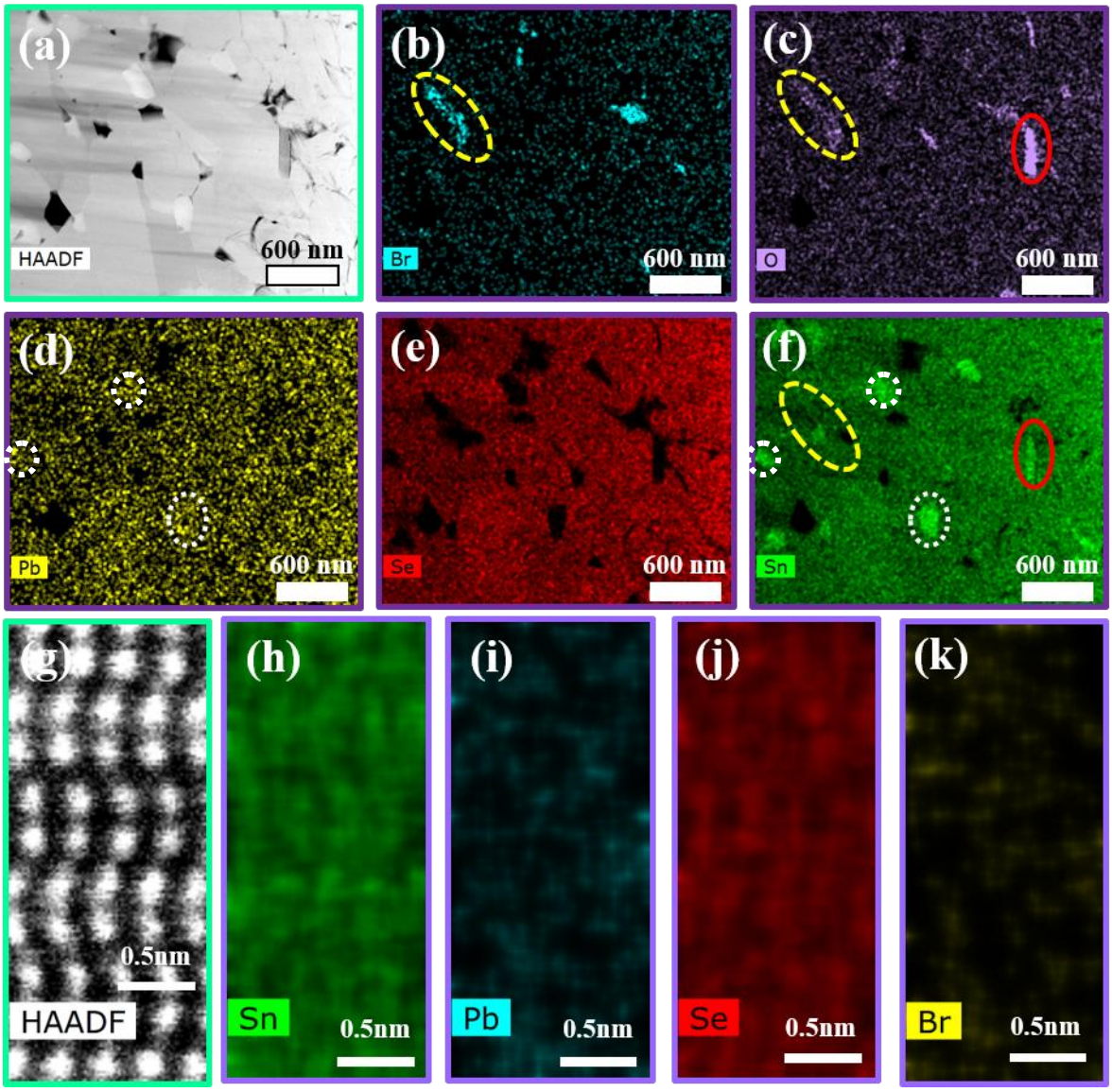
(a)
HAADF
600 nm
(b)
Br
600 nm
(c)
O
600 nm
(d)
Pb
600 nm
(e)
Se
600 nm
(f)
Sn
600 nm
(g)
0.5nm
HAADF
(h)
Sn
0.5nm
(i)
Pb
0.5nm
(j)
Se
0.5nm
(k)
Br
0.5nm

Figure 3.

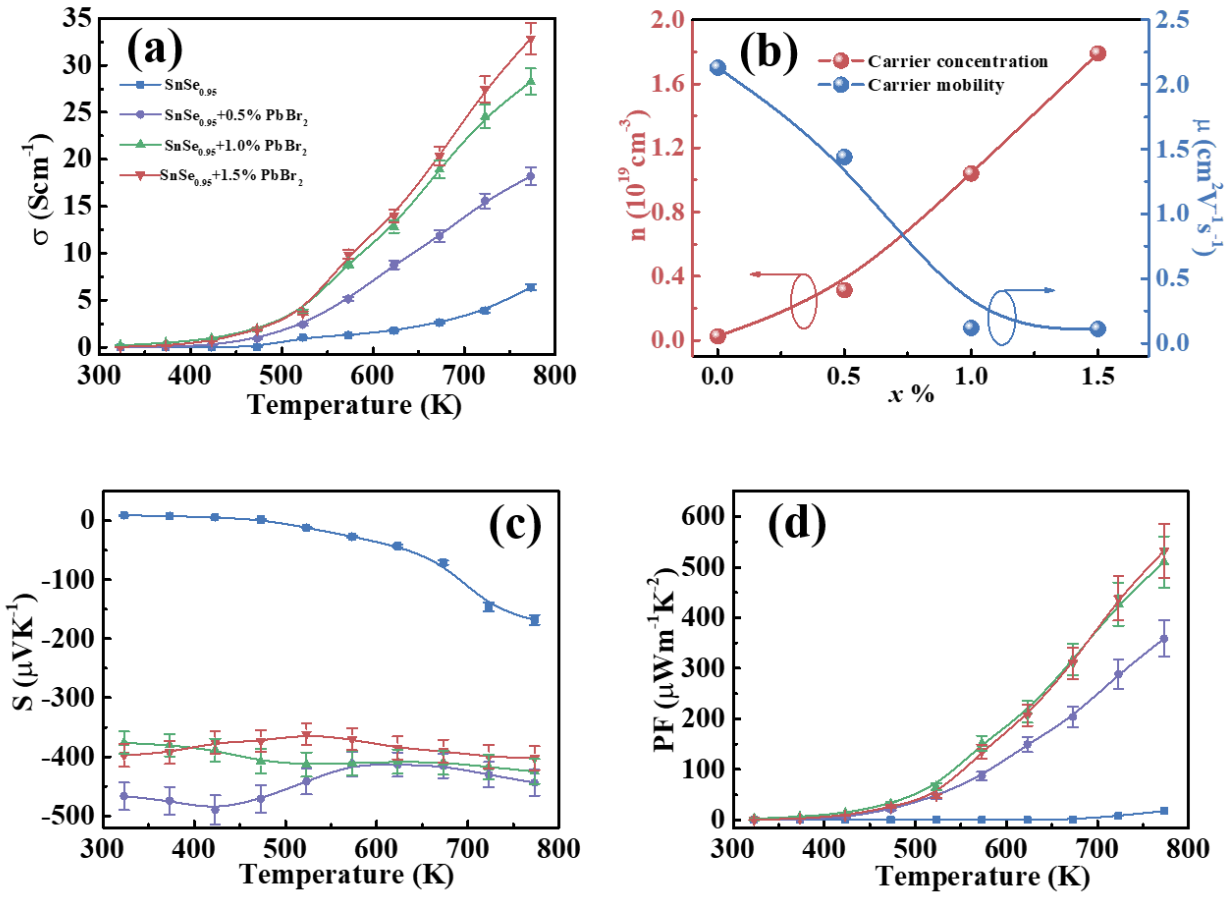
(a)
σ (Scm-1)
Temperature (K)
SnSe0.95
SnSe0.95+0.5% PbBr2
SnSe0.95+1.0% PbBr2
SnSe0.95+1.5% PbBr2
(b)
Carrier concentration
Carrier mobility
n (10^19 cm-3)
μ (cm2V-1s-1)
x %
(c)
S (μVK-1)
Temperature (K)
(d)
PF (μWm-1K-2)
Temperature (K)

Figure 4.

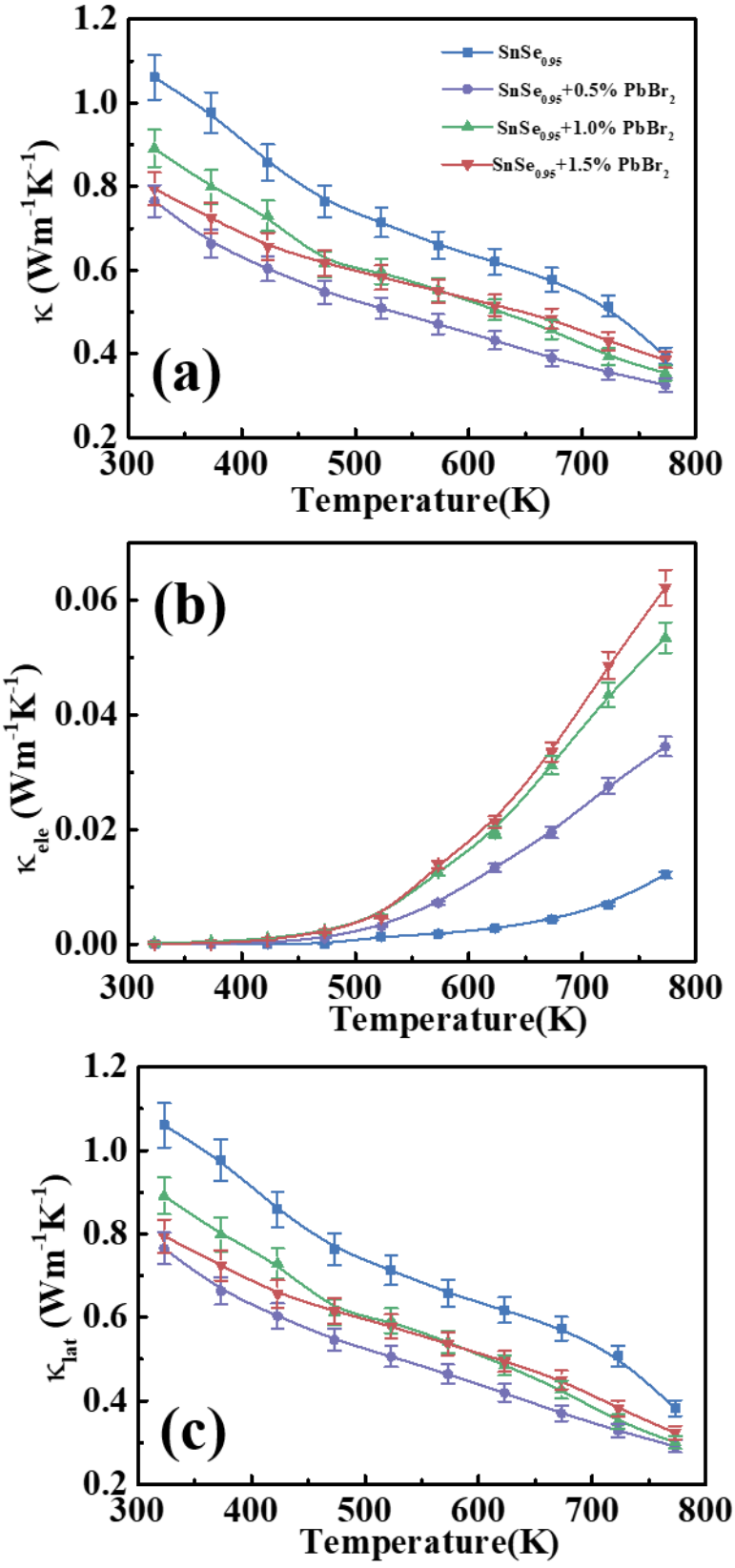
SnSe0.95
SnSe0.95+0.5% PbBr2
SnSe0.95+1.0% PbBr2
SnSe0.95+1.5% PbBr2
(a)
κ (Wm-1K-1)
Temperature(K)
(b)
κele (Wm-1K-1)
Temperature(K)
(c)
κlat (Wm-1K-1)
Temperature(K)

Figure 5.

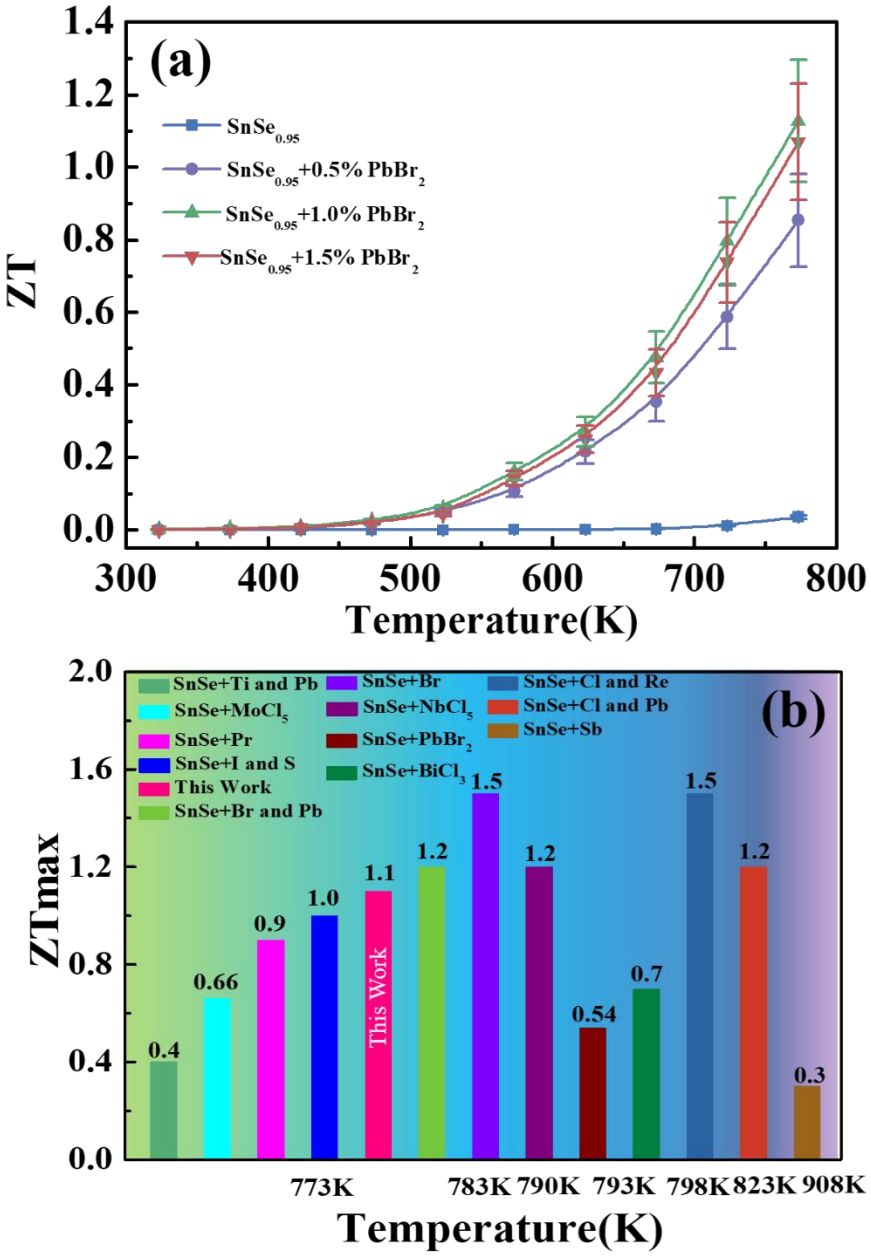
(a)
ZT
Temperature(K)
SnSe0.95
SnSe0.95+0.5% PbBr2
SnSe0.95+1.0% PbBr2
SnSe0.95+1.5% PbBr2
(b)
ZTmax
Temperature(K)
SnSe+Ti and Pb
SnSe+MoCl5
SnSe+Pr
SnSe+I and S
This Work
SnSe+Br and Pb
SnSe+Br
SnSe+NbCl5
SnSe+PbBr2
SnSe+BiCl3
SnSe+Cl and Re
SnSe+Cl and Pb
SnSe+Sb
This Work
773K
783K
790K
793K
798K
823K
908K

Figure 6.